Experimental Investigation of the DLR-F6 Transport Configuration in the National Transonic Facility (Invited)

Gregory M. Gatlin[*] and Melissa B. Rivers[†]
NASA Langley Research Center, Hampton, VA, 23681

Scott L. Goodliff[‡]
Jacobs Sverdrup, Hampton, VA, 23681

and

Ralf Rudnik[§] and Martin Sitzmann[¶]
DLR, German Aerospace Center, D-38112 Braunschweig, Germany

An experimental aerodynamic investigation of the DLR (German Aerospace Center) F6 generic transport configuration has been conducted in the NASA NTF (National Transonic Facility) for CFD validation within the framework of the AIAA Drag Prediction Workshop. Force and moment, surface pressure, model deformation, and surface flow visualization data have been obtained at Reynolds numbers of both 3 million and 5 million. Flow-through nacelles and a side-of-body fairing were also investigated on this wing-body configuration. Reynolds number effects on trailing edge separation have been assessed, and the effectiveness of the side-of-body fairing in eliminating a known region of separated flow has been determined. Data obtained at a Reynolds number of 3 million are presented together for comparison with data from a previous wind tunnel investigation in the ONERA S2MA facility. New surface flow visualization capabilities have also been successfully explored and demonstrated in the NTF for the high pressure and moderately low temperature conditions required in this investigation. Images detailing wing surface flow characteristics are presented.

Nomenclature

b	=	wing span, in
c	=	wing mean aerodynamic chord, in
C_D	=	drag coefficient
C_L	=	lift coefficient
C_m	=	pitching-moment coefficient referenced to 0.25 of the wing mean aerodynamic chord
c_{Nac}	=	wing chord at nacelle location, in
C_p	=	pressure coefficient
CFD	=	computational fluid dynamics
DLR	=	German Aerospace Center
DPW	=	Drag Prediction Workshop
M_∞	=	freestream Mach number
NASA	=	National Aeronautics and Space Administration
NTF	=	National Transonic Facility
R_c	=	Reynolds number based on mean aerodynamic chord

---

[*] Research Engineer, Configuration Aerodynamics Branch, Mail Stop 267, Senior Member AIAA.
[†] Research Engineer, Configuration Aerodynamics Branch, Mail Stop 267, Senior Member AIAA.
[‡] Test Engineer, ROME Group, Mail Stop 267, Senior Member AIAA.
[§] Head Transport Aircraft, Institute of Aerodynamics and Flow Technology, Lilienthalplatz 7
[¶] Test Engineer, Institute of Aerodynamics and Flow Technology, Lilienthalplatz 7

S	=	model reference area, ft^2
WB	=	Wing/Body
WBF	=	Wing/Body/Fairing
x/c	=	longitudinal distance from wing leading edge nondimensionalized by local wing chord
x_{TE}	=	distance in x direction from wing leading edge to nacelle upper trailing edge, in
z_{TE}	=	distance in z direction from wing leading edge to nacelle upper trailing edge, in
α	=	angle of attack, deg
η	=	fraction of wing semi-span
φ	=	angular location of nacelle pressure orifices, 0 is at top, deg

I. Introduction

In an effort to assess the state of the art in computational fluid dynamics (CFD) drag prediction, the AIAA Applied Aerodynamics Technical Committee has initiated a series of Drag Prediction Workshops. The goal of the workshops is to assess state-of-the-art computational methods as practical aerodynamic tools for aircraft force and moment prediction of industry relevant geometries, with the focus being on drag prediction. Furthermore, the Drag Prediction Workshop (DPW) is designed to serve as an impartial forum for evaluating the effectiveness of existing computational Navier-Stokes solvers and modeling techniques. In addition, the DPW forum is intended to promote an open discussion on areas needing additional research and development. In order to encourage the widest participation, public-domain subject geometries have been used that are industry-relevant, yet simple enough to permit high-fidelity computations. Additionally, baseline grids have been provided with the intent of reducing the variability of CFD results.

The first drag prediction workshop[1,2] (DPW-I), held in June of 2001, was directed at the calculation of a wing/body commercial transport configuration, known as the DLR-F4[3,4]. Previously obtained experimental data were available to compare to for this first workshop. Predictions of a cruise polar and the drag rise were the focus. The second drag prediction workshop[5,6] (DPW-II), held in June of 2003, added the challenge of determining the increment due to adding a large component, in this case a pylon/nacelle. The DLR-F6 configuration[5,7] was used for this study. Once again, experimental data were available to compare to. The third drag prediction workshop[8,9] (DPW-III), held in June of 2006, added the challenge of determining the increment due to adding a small component, in this case a wing/body fairing. However for this workshop, the calculations were conducted "blind" with no experimental data available to compare to. It is these "blind" calculations that draw the connection between the third drag prediction workshop and the current experimental investigation. The force and moment, surface pressure, model deformation, and surface flow visualization data obtained in an NTF wind tunnel investigation on the DLR-F6 configuration and the results presented in this paper serve as the validation data for the calculations presented in the DPW-III.

II. Experimental Approach

A. Facility Description

The NTF[10] is a unique national facility (Fig. 1) that enables testing of aircraft configurations at conditions ranging from subsonic to low supersonic speeds at Reynolds numbers up to full-scale flight values. The NTF is a conventional, closed-circuit, continuous-flow, fan-driven wind tunnel (Fig. 2) capable of operating in either dry air at warm temperatures or nitrogen from warm to cryogenic temperatures. Elevated pressures in combination with cryogenic temperatures enable testing to the highest Reynolds numbers. The test section is 8.2 by 8.2 by 25 ft and has a slotted floor and ceiling. In addition, turbulence is reduced by four damping screens in the settling chamber and a contraction ratio of 14.95-to-1 from the settling chamber to the nozzle throat. Fan-noise effects are minimized by acoustic treatment both upstream and downstream of the fan. Thermal insulation resides inside the pressure shell to aid in maintaining tunnel temperature and thus minimize energy consumption.

The NTF has an operating pressure range of approximately 15 to 125 psia, a temperature range of -260 to +120°F, and a Mach number range of 0.2 to 1.2. The maximum Reynolds number per foot is 146 x 10^6 at Mach 1. When the tunnel is operated cryogenically, heat is removed by the evaporation of liquid nitrogen, which is sprayed into the tunnel circuit upstream of the fan. During this operational mode, venting is necessary to maintain a constant total pressure. When air is the test gas, heat is removed from the system by a water-cooled heat exchanger at the upstream end of the settling chamber. Further tunnel details and facility information are provided in Ref. 11.

B. Model Description

The wind tunnel model used in the current investigation was a refurbished DLR-F6 model. This configuration, representative of a modern, twin-engine, transport aircraft, is a transonic speed, wing-body design derived from the earlier DLR-F4 configuration[4]. The DLR-F6 model was originally built in the 1980's and subsequently tested in several investigations at the French ONERA S2MA wind tunnel. The DLR-F6 is designed for a cruise Mach number of $M_\infty = 0.75$ and a corresponding design lift coefficient of $C_L = 0.5$. A three-view sketch of the model showing the overall dimensions is given in Fig. 3. The aspect ratio is 9.5, the leading edge sweep angle is 27.1°, the wing reference area (S) is 1.565 ft², the wing span (b) is 46.114 inches, and the mean aerodynamic chord (c) is 5.559 inches. The model moment reference center is located 19.878 inches back from the fuselage nose and 1.336 inches below the fuselage centerline. The DLR-F6 model originally consisted of a glass fiber reinforced polymer fuselage and a pair of steel wings both of which are bolted to an internal steel balance block. In addition, the DLR-F6 model can be equipped with several different types of flow-through nacelles with 3 different mounting positions. The nacelles chosen for the NTF tests are CFM-type long duct nacelles mounted at position 1 as identified in Ref. 12. The nacelles and pylons are both made of aluminum. The nacelle position is characterized by a distance in the x (positive is streamwise) and z (positive is up) directions between the wing leading edge and the nacelle upper trailing edge (x_{TE}, z_{TE}) in relation to the local wing chord length (c_{Nac}) respectively. Position 1 is represented by $x_{TE} / c_{Nac} = 0.49$ and $z_{TE} / c_{Nac} = -0.189$ with $c_{Nac} = 5.260$ inches. Pressure distributions are measured on the right wing by 288 pressure orifices located in 8 span-wise wing sections ($\eta = 0.150, 0.238, 0.331, 0.377, 0.409, 0.512, 0.635$ and 0.844), on the left nacelle by 47 orifices in 3 radial sections ($\varphi = 60°$, 180° and 300°), and on the left pylon by orifices in 9 locations. All pressure measurements were made using Electronically Scanned Pressure (ESP) modules mounted inside the forward portion of the fuselage. Based on quoted accuracies from the ESP module manufacturer, surface pressure measurements should be in error by no more than +/- 0.015 psi. This in turn would correspond to a variation of no more than +/- 0.0026 in terms of C_p. The model is mounted in the wind tunnel using a blade sting arrangement as illustrated in Fig. 3. A photograph of the DLR-F6 model as it was mounted in the test section of the NTF is presented in Fig. 4.

The original DLR-F6 model was designed for atmospheric test conditions and had been previously tested up to a Reynolds number of 3 million based on mean aerodynamic chord. The current investigation however, called for testing at both 3 and 5 million Reynolds number. This increased Reynolds number would require either increasing the total pressure or decreasing the total temperature or a combination of both. The DLR-F6 model is not capable of withstanding full cryogenic low temperature conditions, therefore increased pressurization was initially viewed as the more favorable process to provide the desired Reynolds number increase during the NTF test.

Due to the fact that the increased aerodynamic loads resulting from an increased total pressure were expected to exceed the design limits of the original model, it had to be determined to what extent the model could withstand the corresponding increased dynamic loads. In addition, the stress safety factors as defined by the test facility had to be maintained. Thus in order to properly address these issues, DLR performed a load and stress analysis using fluid-structure coupled simulations on the original wing. A considerable reduction of stress levels and wing deformation was found in comparison to a preliminary conventional analysis using aerodynamic loads from the undeformed model geometry. Structural loads further decreased with either a reduction of ambient temperature, Reynolds number or lift coefficient with all other conditions remaining the same. Lowering the tunnel temperature was found to yield the largest structural loads reduction while maintaining the desired test Reynolds number of 5 million[13].

During initial model preparations, DLR refurbished the DLR-F6 model in order to account for the increased aerodynamic forces and the resulting structural loads. A new fuselage consisting of two half-shells made of 10 layer carbon fiber reinforced polymer (CFRP) was designed and manufactured. Aluminum attachment brackets securely bonded to the inside of the fuselage skins were used to attach the half-shells to the balance block. On top of the left half-shell, 8 pressure orifices were installed near the centerline. Each half-shell had a cutout in the region of the wing-fuselage junction and in the region of the blade sting interface to incorporate inserts. The new fuselage was equipped with two interchangeable sets of inserts made of carbon fiber composite to be positioned at the wing-fuselage junction. One set had the shape of the original DLR-F6 cylindrical fuselage and the other had the shape of the FX2B fairing[14] (Fig. 5) (this is the wing/body fairing analyzed in the third drag prediction workshop). Each set of inserts consisted of 4 parts (upper/lower, left/right). On each set, pressure orifices were installed on the upper inserts in the region of the wing-fuselage flow separation, 10 on the left side and 4 on the right side of the model. A change from the configuration without the fairing to the configuration with the FX2B side-of-body fairing was done easily by exchanging the set of inserts.

In addition to the new model components just described, NASA had a new blade sting designed and built for the installation of the DLR-F6 model in the NTF. Not only did this blade sting provide the proper interface between NASA's NTF-104B strain gauge balance and the NTF arc sector model support structure, it also was designed to

match as closely as possible the blade sting used in the previous tests in the ONERA S2MA wind tunnel. Due to the higher load requirements for the NTF test, the blade on the new NASA sting was approximately 1.3 inches longer, in the streamwise direction, and approximately one-eighth inch wider (at the location where it enters the fuselage). A new balance block was built by DLR to provide the appropriate interface for the balance and the fuselage attachment components. Based on the results of a finite-elements analysis, the junction between both wings and the balance block was reinforced. A set of sting blade inserts made of carbon fiber composite and shaped close to the surface of the NTF sting blade was prepared by DLR. During the final test preparation at the NTF, the gap between the fuselage inserts and the sting blade was carefully sealed by use of a small custom-made glass fiber fabric seal. Special care was taken to ensure the gap was sealed without creating any forces between the non-metric sting blade and the metric fuselage inserts. An illustration of the main components of the DLR-F6 model as it was mounted to the new NTF sting is presented in Fig. 6.

C. Test Conditions

The investigation, conducted over a 4-week period, provided force and moment, surface pressure, model deformation, and surface flow visualization data. Testing was conducted at 3 million Reynolds number in order to compare with previously existing data and also at 5 million Reynolds number such that an assessment of Reynolds number effects could be made (albeit over a small range). All Reynolds number values presented in this paper are based on mean aerodynamic chord. Due to strength limitations of the model and the requirement to obtain data at an increased Reynolds number of 5 million, all testing was conducted at a freestream total temperature of 40°F in nitrogen gas. Testing at this moderately reduced temperature allowed for a 5 million Reynolds number condition without requiring a dynamic pressure that would have exceeded model strength limitations.

All data presented in this paper were obtained at a freestream Mach number of 0.75. Data were generally obtained over an angle-of-attack range from -4° to +2° at 3 million Reynolds number and from -4° to +1° at 5 million Reynolds number. The reduced angle-of-attack range at 5 million Reynolds number was required such that safe model stress levels would not be exceeded. Flow angularity measurements were made and upflow corrections ranging from 0.15° to 0.185° were applied to the final data. Classical wall corrections accounting for model blockage, wake blockage, tunnel buoyancy, and lift interference have been applied according to the methods presented in Ref. 15. Testing on the Wing/Body/Nacelle/Pylon configuration was conducted at a Reynolds number of 3 million only. However, data were obtained at both 3 and 5 million Reynolds number for both the Wing/Body and Wing/Body/Fairing configurations.

In order to ensure a consistent and repeatable transition from laminar to turbulent flow and to support the goal of the wind tunnel data being used for CFD validation purposes, it was important to apply a proven and reliable method to fix transition on the model. Vinyl adhesive trip dots measuring 0.05 inches in diameter and spaced 0.1 inches apart (center to center) have been applied routinely on models at the NTF for flow transition and were used for the current investigation. A trip dot height of 0.0040 inches was used on the model for all testing conducted at 3 million Reynolds number. These trip dots were applied at the nose of the fuselage and on both the upper and lower surfaces of the wings at the same locations as illustrated in Ref. 4. When the nacelles were on the model, trip dots were located 0.47 inches back from the leading edge on the outer surface and 0.59 inches back from the leading edge on the inner surface. This trip dot application arrangement was used because it was the same as that used when the DLR-F6 model was previously tested at 3 million Reynolds number at the ONERA S2MA wind tunnel. When testing at a Reynolds number of 5 million, the trip dots on the wing were changed to a height of 0.0031 inches and were located at 10-percent of the local chord back from the leading edge on the trapezoidal wing planform. Effectiveness of the transition application was confirmed at both Reynolds numbers by conducting an initial run with the trip dot region covered with a sublimating chemical coating. An initial sublimation of the coating off the model surface just downstream of the trip dots confirmed the desired transition of the flow from laminar to turbulent.

A surface oil flow visualization technique was also used in the investigation to effectively provide additional detailed insight into the flowfield over the model surface. After experimenting with several different levels of oil viscosity, different fluorescent dye mixtures, and various camera and flash adjustments, an effective surface flow visualization capability was developed for the test conditions of interest. The somewhat non-standard test temperature of 40°F added to the challenge of the development effort. A mixture of oil and fluorescent dye was applied with a paintbrush in a very light coating over the entire upper surface of the non-pressure-instrumented (left) wing, and then the tunnel test condition was set as quickly as possible. Multiple video images were captured from cameras mounted in the tunnel wall and ceiling. A longtime reluctance to introducing surface oil flow visualization to the NTF had been the standard philosophy due to the concern that any oil leaving the model surface could have detrimental effects should it be absorbed into the interior tunnel insulation and later come loose in solid form during

subsequent cryogenic operations. In order to reduce this concern, oil was used sparingly and a thorough tunnel cleaning, aided due to the fluorescence of the oil, was conducted after the investigation was complete. An additional benefit to the cleanup process was the fact that any residual oil that left the model tended to stay on the centerline of the tunnel circuit and collect on turning vanes, nitrogen injectors, or the upstream portion of the drive fan nacelle and not on the insulation on the interior walls. As a result of this successful flow visualization portion of the test, the NTF can now offer a surface oil flow visualization capability to future clients.

Another important set of data obtained in this investigation was model deformation measurements. Since an effective correlation of computational and experimental data will be directly tied to how well the computational and experimental model geometries match one another, it is important to obtain an accurate definition of the model geometry as tested under aerodynamic loads. In order to obtain this information a video model deformation measurement technique[16] has been developed and employed multiple times at the NTF. This system was used in the current investigation to obtain wing deflection and twist measurements due to aerodynamic loading. The results obtained from these measurements are presented in Ref. 17.

III. Results and Discussion

A. Comparison of NTF and ONERA Data

One of the goals of the current investigation was to obtain data in the NTF at the same conditions as data previously obtained with the DLR-F6 model in the ONERA S2MA wind tunnel. Data at these conditions, $M_\infty = 0.75$ and $R_c = 3$ million, were obtained at the NTF and are presented for comparison with the ONERA data[18] in Fig. 7 for the Wing/Body configuration. When comparing the longitudinal aerodynamic data, a reasonably good agreement is observed, however some differences are noted. Lift, drag, and pitching moment coefficients from the NTF are all slightly lower than those from the ONERA test. Over the angle-of-attack range investigated, lift coefficients are on the order of 0.01 to 0.02 less than in the ONERA data. It is generally thought this relatively small difference would be accepted as reasonable in a wind tunnel-to-wind tunnel comparison, especially with the tests being conducted approximately 17 years apart. The wing pressure data at design C_L, shown at four spanwise stations in Fig. 7(b), are also in relatively good agreement. While the inboard pressure distributions match quite well, some differences are found on the forward part of the outboard portions of the wing, on both upper and lower surfaces. The outboard NTF data indicate a higher pressure differential over the forward portion of the wing than that indicated by the Onera data. These small variations however, could be attributed to the slight difference in lift coefficient of about two percent between the two data sets. It should also be noted that some pressure orifices were not operational in one test or the other.

The NTF pitching-moment coefficient (shown in Fig. 7(a)) is approximately 0.0015 below the ONERA value at -4° angle of attack; however, this difference is consistently reduced as angle of attack is increased, with the pitching-moment data matching the ONERA data at approximately 1.5° angle of attack. One possible explanation for this difference is the fact that a different type of metric to non-metric seal was used at the sting blade-to-fuselage interface. Since the center of the sting blade is approximately 18 inches aft of the model moment reference center, a difference in normal force at the blade seal of only 0.6 pounds could account for the maximum noted difference in pitching moment. Thus the noted pitching-moment difference would seem acceptable when such a small force at a relatively large distance could account for the variation. The previously mentioned pressure differences on the forward portion of the outboard wing correlate with the pitching-moment offset, and thus could also explain the difference. Another possible contributor to the NTF nose-down pitching-moment increment is the fact that the NTF sting blade is both longer and wider than the one used in the ONERA investigation. This could result in a lower pressure region around the NTF sting blade as the local flow must accelerate around this larger structure. This lower pressure on the upper aft end of the fuselage could in turn translate into an increment in nose-down pitching moment.

When the drag coefficient data are compared there is a difference in minimum drag on the order of ten drag counts. This difference was more than one would expect, thus further investigation as to the reason why was pursued. Upon investigating corrections applied to the ONERA data, it was determined that a sting correction to axial force was being applied, whereas a sting correction to the NTF data was not available at the time of the data analysis. At the minimum drag coefficient, the ONERA sting correction increased drag by 11 drag counts. This correction applied to the ONERA data would then account for the offset noted in the drag coefficient data.

Presented together in Fig. 8 are NTF and ONERA data for the Wing/Body/Nacelle/Pylon configuration. As expected the typical engine/airframe interference effects are well reproduced in the NTF. The longitudinal data, when compared to the Wing/Body configuration data of Fig. 7(a), show the addition of the nacelles and pylons

changes the character of the pitching moment, slightly reduces the lift curve slope, and results in minimum drag occurring at a higher lift-coefficient value. The accelerated flow on the underside of the wing at $\eta = 0.331$ due to the presence of the nacelle and pylon is well captured in the pressure data from both facilities (Fig. 8(b)). Small differences in the overall wing pressure distributions are again likely attributed to the slight difference in lift coefficient between the two data sets. Outboard NTF pressure data again indicate a higher pressure differential over the forward portion of the wing. All NTF longitudinal data are still slightly lower than those from the ONERA test. In general however, the same facility comparison trends as noted above for the Wing/Body configuration are again present.

B. Reynolds Number Effects

Another goal of the current investigation was to extend the database from a Reynolds number of 3 million up to 5 million such that an assessment of Reynolds number effects could be made. It is recognized this Reynolds number range is relatively small, in comparison to flight Reynolds numbers, thus Reynolds number effects may be limited. Data have been obtained at both 3 and 5 million Reynolds number for the Wing/Body configuration, and these data are presented together for comparison in Fig. 9. Upon examination of the lift coefficient data, it would appear there is essentially no Reynolds number effect. However, Reynolds number effects are clearly seen for both drag and pitching moment.

In general, for a constant angle of attack, an increase in Reynolds number primarily leads to an increase in lift due to a thinner boundary layer and thus an increased effective camber of the wing. In the current data set however, with temperature being held constant at 40°F, increased Reynolds number comes along with increased dynamic pressure and in turn static aeroelastic effects. Aeroelastic effects due to the increased dynamic pressure at 5 million Reynolds number result in an increased nose-down wing twist, which would in turn act to reduce lift. Thus the lack of any noticeable Reynolds number effect on the lift coefficient data presented is likely due to offsetting Reynolds number and static aeroelastic effects. This trend of offsetting Reynolds number and static aeroelastic effects has been encountered in previous investigations in the NTF and is documented in Ref. 19.

As Reynolds number is increased, a reduction in drag is noted, with this reduction being nearly uniform across the range of lift coefficient presented. This uniform reduction would thereby be attributed to a reduction in the viscous drag. At the point of minimum drag, the increased Reynolds number results in a 10-count reduction in drag coefficient. In addition, as Reynolds number is increased there is an increase in nose-down pitching moment, with this increment in nose-down pitching moment continuing to increase with increasing angle of attack. Wing pressure distributions at four spanwise locations are presented for both the 3 and 5 million Reynolds number conditions in Fig. 9(b). These data are presented for a nominal lift coefficient of 0.5, with the respective lift coefficients varying by just under 4 percent. The pressure data indicate a slight reduction in lift (reduced pressure peak) on the forward portion of the wing when Reynolds number is increased from 3 to 5 million, with the largest reduction occurring at the most outboard location. This would be consistent with the aeroelastic effects as described above and would support the expectation that static aeroelastic effects would cause the largest nose-down wing twist at the most outboard location. The slightly lower angle of attack for the 5 million Reynolds number data is also recognized as a possible factor contributing to the differences in the pressure data.

Additional insight was obtained in regard to Reynolds number effects through the use of a new surface oil flow visualization technique at the NTF. As described earlier, a mixture of oil and fluorescent dye was applied to the wing in a thin coating with a paintbrush. The tunnel was closed, conditions were quickly set, and multiple images were captured with the wind tunnel camera systems. A 2-inch long row of chordwise and 1-inch long row of spanwise tick marks were placed on the inboard aft portion of the wing in a region of known separated flow to aid in assessment of the size of this separated flow region. A sketch illustrating the exact placement of the tick marks is presented in Fig. 10.

Top-view images, presented in Fig. 11, and rear ¾-view images, presented in Fig. 12, show flow patterns on the wing for both 3 and 5 million Reynolds number conditions. Both sets of images are presented for a lift coefficient of 0.5. Due to the illumination of the fluorescent dye in the oil it is noted that light regions in the flow visualization images indicate the presence of oil and dark regions indicate the absence of oil. Careful examination of these images reveals multiple details of the wing upper surface flow patterns. The inboard flow separation region on the aft portion of the wing is clearly visible. The spanwise extent of the separated flow region appears to be very similar when the 3 and 5 million Reynolds number conditions are compared. Slightly more oil is in the separated flow region for the 5 million Reynolds number images, however this does not indicate a specific difference in the separated flow between the two Reynolds numbers. There does however appear to be a difference in the length of the separated flow region. The separated flow appears to begin further upstream at 3 million Reynolds number than it does for 5 million Reynolds number. Thus increasing Reynolds number delays the onset of the side-of-body flow

separation, as might be expected due to smaller boundary layer thicknesses on the wing and body respectively. It is also interesting to note evidence of the existence of a horseshoe, or juncture, vortex[20-22] on the wing beside the fuselage. This evidence consists of a dark region on the fuselage around the wing where most of the oil has been scrubbed off the fuselage (typical of a horseshoe vortex) and a region on the wing right at the side of the fuselage where most of the oil has again been scrubbed away. The surface flow patterns would indicate the vortex is either smaller or has less of an interaction with the wing upper surface as Reynolds number is increased from 3 to 5 million. This is particularly evident right at the beginning of the separated flow region.

Another effect of an increase in Reynolds number, as illustrated by the surface flow visualization, is a reduction in wing trailing-edge separation. This is seen in the images presented in Fig. 11 in a narrow area just outboard of the wing kink, and although difficult detect in the images presented, it also occurs to a lesser extent inboard of this point. The very narrow region completely void of oil right at the wing trailing edge and the larger region of pooled oil just upstream of it in the image for 3 million Reynolds number indicate a greater region of wing trailing edge separation when compared to the image for 5 million Reynolds number. Also evident in the flow visualization is the location of the shock on the forward portion of the wing at up to roughly 20-percent of the local chord, depending on span. The rear ¾-view images (Fig. 12) were obtained with a higher resolution camera and therefore show more details within the side-of-body separated flow region. These images show evidence of the counterclockwise swirling of the flow in the side-of-body separated flow region that was easily visible when viewing the actual flow visualization pattern formations during the test. Although difficult to see in these images, there is also evidence of flow separation on the side of the fuselage near the wing trailing edge at both Reynolds numbers. One final point of observation is the streaks in the oil flow pattern that extend downstream from each of the trip dots. These streaks help to provide an indication of local surface flow direction.

C. Comparison of Wing/Body and Wing/Body/Fairing Configurations

Another important part of the investigation was to assess the effects resulting from adding the FX2B side-of-body fairing. This fairing was specifically designed to eliminate the known side-of-body separation just addressed in the previous flow visualization images. An illustration showing the shape and position of the FX2B fairing installed on the DLR-F6 model is presented in Fig. 5. Longitudinal force and moment and wing surface pressure data are presented for both the Wing/Body and Wing/Body/Fairing configurations in Fig. 13. Upon examination of the force and moment data, the addition of the fairing is shown to produce a reduction in lift, a reduction in drag, and a nose-up increment in pitching moment. The reduction in lift coefficient is on the order of 0.017 at the lowest angle of attack, with this increment being reduced slightly as angle of attack is increased. Part of this lift reduction would likely be due to the fairing now covering a portion of the wing. The portion of the fairing covering the aft part of the wing would in turn account for an increment in nose-up pitching moment. The drag reduction indicates the desired effectiveness of the fairing in reducing the extent of the separated flow region. In the region of minimum drag, the addition of the fairing results in a reduction in drag on the order of 3 counts. This same drag increment generally holds across the angle-of-attack range investigated, although there is slightly more variation in the drag data at the higher angles of attack.

An assessment of the wing pressure data helps to provide further insight as to the causes for the nose-up increment in pitching moment. To aid in the evaluation of the fairing influence, pressure data are presented at the four most inboard span stations for both configurations (Fig. 13(b)). These data indicate effects of the fairing can be seen out to the second row of pressure orifices; however, effects beyond that, if any, are minimal. The presence of the fairing is shown to create an increased flow velocity over the first 25-percent of the wing upper surface at the first two span stations. This effect would produce an increment in nose-up pitching moment. At the first two span stations it is also noted that the presence of the fairing produces a lower pressure region along most of the wing lower surface. This is not unexpected since the fairing effectively increases the size of the fuselage along the entire undersurface of the wing (see Fig. 5). This effect would in turn account for the small reduction in lift coefficient. The largest effect of the fairing on the pressure data is seen on the aft end of the most inboard pressure row. A reduced pressure on both the upper and lower surfaces indicates the effectiveness of the fairing in eliminating the separated flow region. These pressure data also indicate a small reduction in lift, which due to the aft location would provide an increment in nose-up pitching moment.

Surface flow visualization images illustrating the effects of the side-of-body fairing are presented in Figs. 14 and 15. These images are all presented for a Reynolds number of 5 million and a lift coefficient of 0.5. Images for the Wing/Body configuration are presented again in part (a) of these figures such that an easy assessment of the effects of adding the fairing can be made. Both the top-view and rear ¾-view images clearly show the effectiveness of the fairing in eliminating the side-of-body separated flow region. Smooth attached flow over the top of the fairing is easily visible. Also noted is the effect of the side-of-body fairing on the wing-body juncture flow. The wing-body

juncture vortex is clearly influenced by the presence of the side-of-body separation region on the Wing/Body configuration. In this case the juncture vortex may be lifted away from the wing surface, or pushed outboard, or both, when it comes in contact with the separated flow region. It may also be partially or fully absorbed into the separated flow, but in any case, once the separated flow region is encountered, the juncture flow interaction with the wing is changed. When the fairing is added the juncture vortex is pushed outboard around the edge of the fairing, but stays well defined and in contact with the wing surface. Some evidence of a secondary juncture vortex, even further outboard, is also noted. These flow observations would suggest that future off-surface flow visualizations or velocity measurements could add significant insights into the wing-body juncture flow details both with and without the wing-body fairing.

D. Data Repeatability

When data are obtained in any experimental investigation it is important to make an assessment of data accuracy or data repeatability. In order to make such an assessment for the current investigation, multiple repeat runs were obtained for both the Wing/Body and Wing/Body/Fairing configurations. To obtain the most reliable assessment of data repeatability it is best to have the repeat runs distributed widely throughout the duration of the investigation. Unfortunately this process is usually in conflict with an efficient execution of the test plan. Keeping these thoughts in mind, the following sets of repeat runs were obtained. Two series (sets of runs) were conducted for each configuration, with each series consisting of 12 individual runs at multiple test conditions. Within each series, 3 runs were obtained at $M_\infty = 0.75$ and $R_c = 5$ million. Each of these 3 runs were always separated by at least one run at a different test condition. When a series was complete, the tunnel was opened, the model was inspected to ensure nothing had changed, and then the series was repeated. This resulted in 6 repeat runs for the Wing/Body configuration and 6 repeat runs for the Wing/Body/Fairing configuration at our condition of interest, $M_\infty = 0.75$ and $R_c = 5$ million. The repeatability data resulting from these runs are presented in Fig. 16. Delta coefficient data are presented versus angle of attack for both configurations. The delta coefficient data presented represent the difference between the coefficient value measured and the average value of the coefficient at that particular angle of attack. These delta coefficient, or residual, data show the level of variation in the repeat runs. The dotted lines shown on each plot indicate the 3-sigma limits based on all the data across the angle-of-attack range. Thus it is shown that essentially all the residual data fall within the 3-sigma limits.

IV. Summary

Refurbishment of the DLR-F6 model along with the fabrication of a new blade sting have led to the successful completion of a wind tunnel investigation in the National Transonic Facility in a joint effort between NASA and DLR. Data have been obtained at chord Reynolds numbers of both 3 and 5 million for the Wing/Body and Wing/Body/Fairing configurations. Data have also been obtained at a chord Reynolds number of 3 million for the Wing/Body/Nacelle/Pylon configuration. Force and moment, surface pressure, and surface flow visualization data have been presented. Comparisons have been made between NTF and previously obtained Onera S2MA wind tunnel data. Reynolds number effects and the effects of a side-of-body fairing have also been assessed.
1) Results have shown a reasonably good correlation of NTF data with Onera S2MA data once a sting correction has been accounted for.
2) Increases in chord Reynolds number from 3 to 5 million have been found to slightly delay the onset of the known side-of-body separation and also to reduce a short length of separated flow on the upper surface of the wing at the trailing edge.
3) The side-of-body fairing effectively eliminates the original separated flow region and appears to reposition vortex flow in the wing-body juncture region.
4) A newly developed surface oil flow visualization technique at the NTF has effectively shown detailed insights into the wing-body juncture and separated flow regions. This in turn would suggest a future off-body flow investigation would provide an enhanced understanding of these flow characteristics.

Acknowledgments

References

[1]Levy, D. W., Vassberg, J. C., Wahls, R. A., Zickhur, T., Agrawal, S., Pirzadeh, S., and Hemsch, M. J., "Summary of Data from the First AIAA CFD Drag Prediction Workshop," AIAA Paper 2002-0841, January 2002.

[2]Hemsch, M. J., "Statistical Analysis of CFD Solutions from the Drag Prediction Workshop," AIAA Paper 2002-0842, January 2002.

[3]Redeker, G., Schmidt, N., and Müller, R., "Design and Experimental Verification of a Transonic Wing for a Transport Aircraft," *Proceedings of the FDP Symposium on Subsonic/Transonic Configuration Aerodynamics*, AGARD CP 285, 1980, pp. 13.1-13.7.

[4]Redeker, G., "DLR-F4 Wing Body Configuration," *A Selection of Experimental Test Cases for the Validation of CFD Codes*, AGARD Report AR-303, Vol. 2, 1994, pp. B4-1-21.

[5]Laflin, K. R., Vassberg, J. C., Wahls, R. A., Morrison, J. H., Brodersen, O., Radowitz, M., Tinoco, E. N., and Godard, J., "Summary of Data from the Second AIAA CFD Drag Prediction Workshop," AIAA Paper 2004-0555, January 2004.

[6]Hemsch, M. J. and Morrison, J. H., "Statistical Analysis of CFD Solutions from the 2nd Drag Prediction Workshop," AIAA Paper 2004-0556, January 2004.

[7]Rossow, C.-C., Godard, J.-L., Hoheisel, H., and Schmitt, V., "Investigations of Propulsion Integration Interference Effects on a Transport Aircraft Configuration," *Journal of Aircraft*, Vol. 31, No. 5, 1994, pp. 1022-1030.

[8]Vassberg, J. C., Tinoco, E. N., Mani, M., Broderson, O. P., Eisfeld, B., Wahls, R. A., Morrison, J. H., Zickuhr, T., Laflin, K. R., and Mavriplis, D. J., "Summary of the Third AIAA CFD Drag Prediction Workshop," AIAA Paper 2007-0260, January 2007.

[9]Morrison, J. H. and Hemsch, M. J., "Statistical Analysis of CFD Solutions from the Third AIAA Drag Prediction Workshop," AIAA Paper 2007-0254, January 2007.

[10]Gloss, B. B., "Current Status and Some Future Test Directions for the US National Transonic Facility. Wind Tunnels and Wind Tunnel Test Techniques," *Royal Aeronautical Society*, 1992, pp. 3.1-3.7.

[11]Fuller, D. E., "Guide for Users of the National Transonic Facility," NASA TM-83124, 1981.

[12]Brodersen, O. and Stürmer, A., "Drag Prediction of Engine-Airframe Interference Effects Using Unstructured Navier-Stokes Calculations," AIAA Paper 2001-2414, June 2001.

[13]Keye, S., Sitzmann, M., Brodersen, O., and Heinrich, R., "Fluid-Structure Coupled Loads Analysis of DLR's F6 Wing-Body Configuration," AIAA Paper 2008-675, January 2008.

[14]Vassberg, J. C., Sclafani, A. J., and DeHaan, M. A., "A Wing-Body Fairing Design for the DLR-F6 Model: A DPW-III case study," AIAA Paper 2005-4730, June 2005.

[15]Iyer, V., "A Wall Correction Program Based on Classical Methods for the National Transonic Facility (Solid Wall or Slotted Wall) and the 14x22-Ft Subsonic Tunnel at NASA LaRC." NASA/CR-2004-213261, October 2004.

[16]Burner, A. W. and Liu, T., "Videogrammetric Model Deformation Measurement Technique," *Journal of Aircraft*, Vol. 38, No. 4, July-August 2001, pp. 745-754.

[17]Burner, A. W., Goad, W. K., Massey, E. A., Goad, L. R., Goodliff, S. L., and Bissett, O. W., "Wing Deformation Measurements of the DLR-F6 Transport Configuration in the National Transonic Facility," AIAA Paper 2008-6921, August 2008.

[18]http://aaac.larc.nasa.gov/tsab/cfdlarc/aiaa-dpw/Workshop2/wind_tunnel_data.html

[19]Wahls, R. A., Gloss, B. B., Flechner, S. G., Johnson, W. G., Jr., Wright, F. L., Nelson, C. P., Nelson, R. S., Elzey, M. B., and Hergert, D. W., "A High Reynolds Number Investigation of a Commercial Transport Model in the National Transonic Facility," NASA TM-4418, 1993.

[20]Visbal, M. R., "Structure of Laminar Juncture Flows," *AIAA Journal*, Vol. 29, No. 8, August 1991, pp. 1273-1282.

[21]Baker, C. J., "The Laminar Horseshoe Vortex," *Journal of Fluid Mechanics*, Vol. 95, Part 2, 1979, pp. 347-367.

[22]Pierce, F. J. and Harsh, M. D., "The Mean Flow Structure Around and Within a Turbulent Junction or Horseshoe Vortex – Part II. The Separated and Junction Vortex Flow," *Journal of Fluids Engineering*, Vol. 110, December 1988, pp. 415-423.

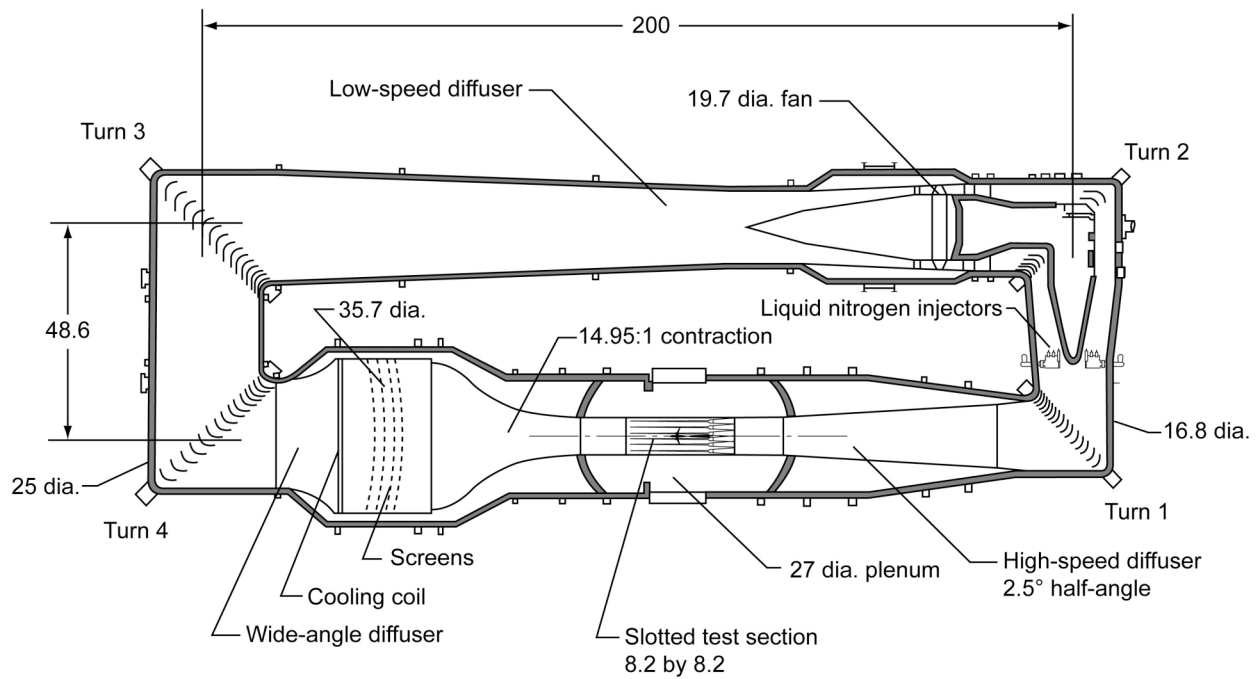**Figure 1. Aerial view of the National Transonic Facility.**

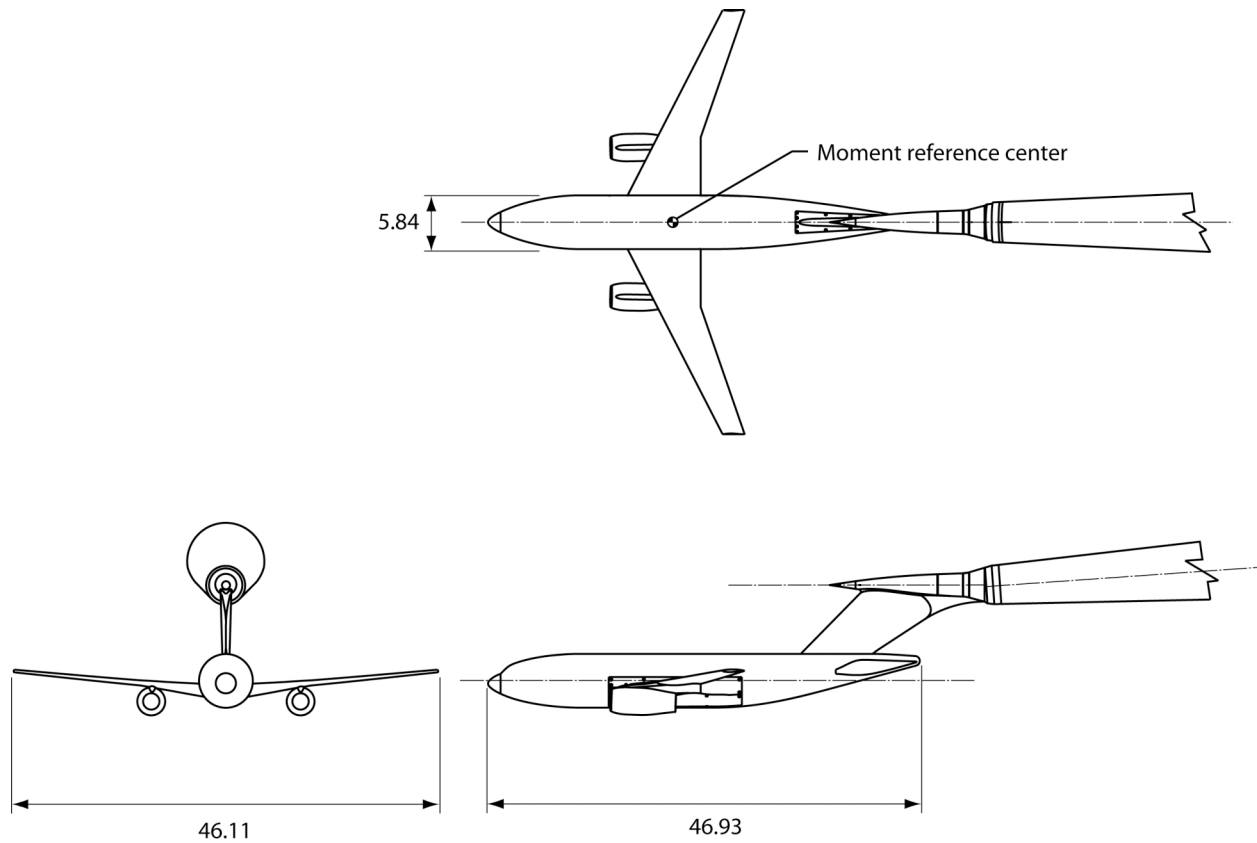**Figure 2. Sketch of the National Transonic Facility tunnel circuit. Linear dimensions are given in feet.**

Figure 3. Three-view sketch of the DLR-F6 model. Dimensions are given in inches.
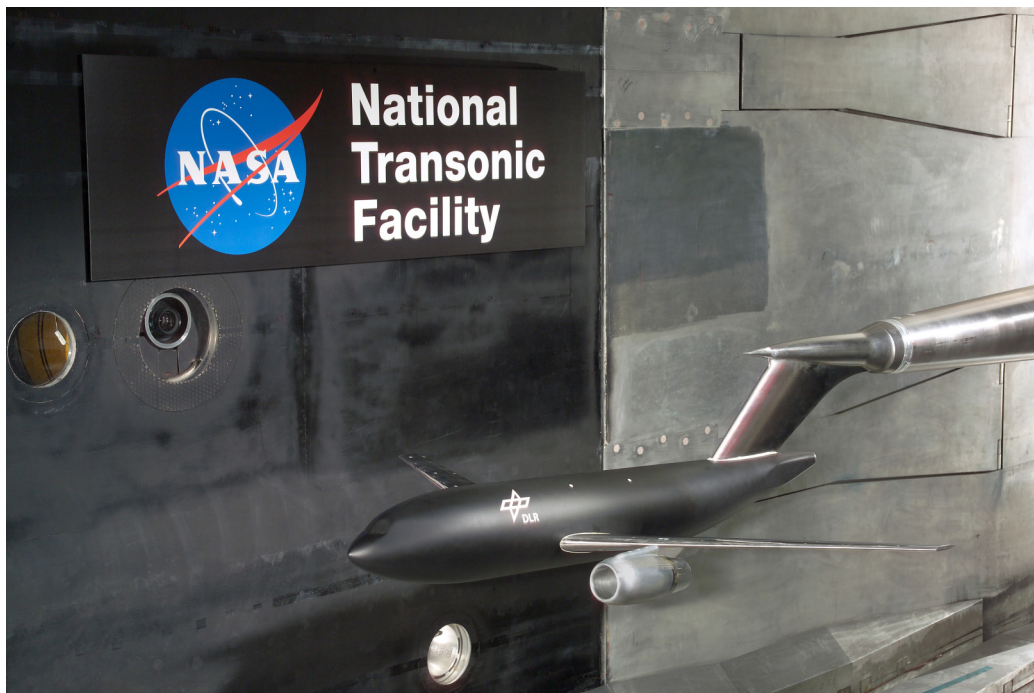

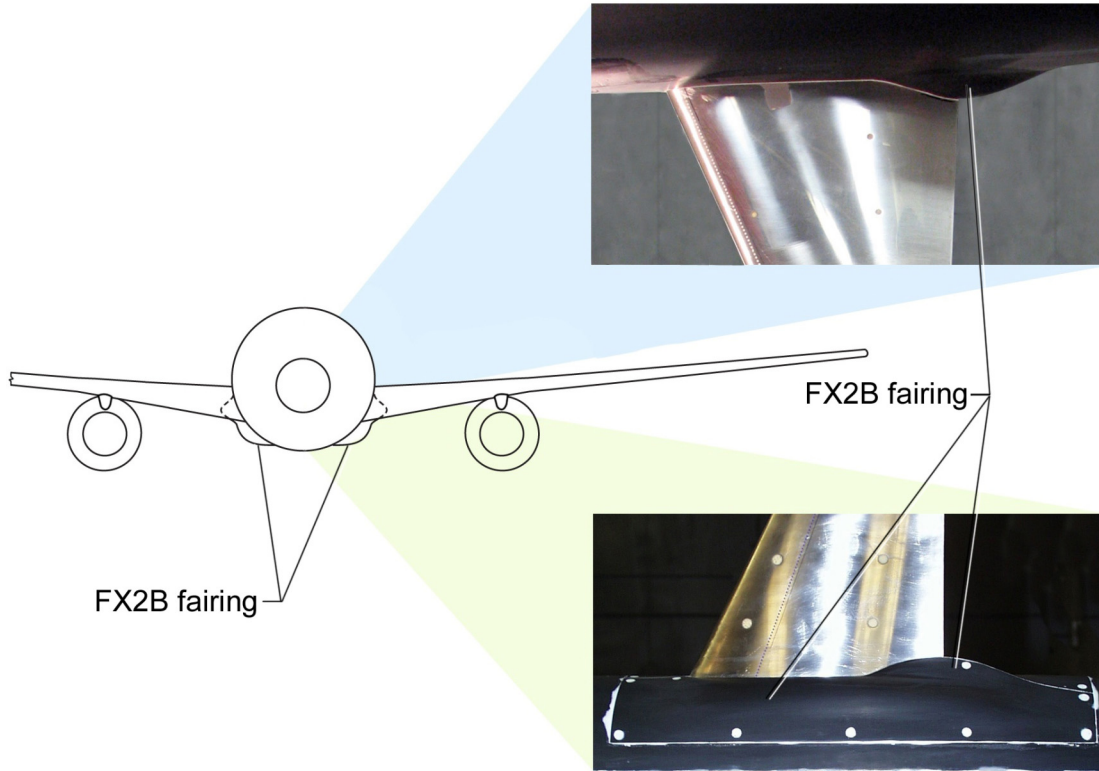**Figure 4. Photograph of the DLR-F6 model mounted in the test section of the National Transonic Facility.**

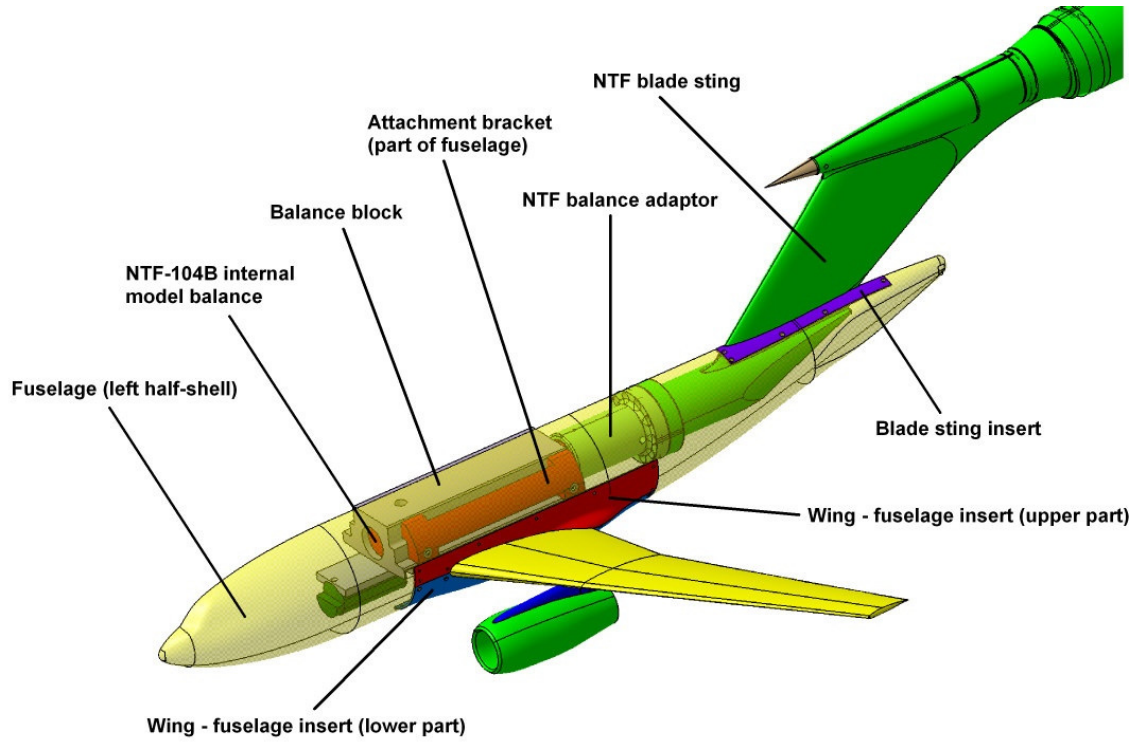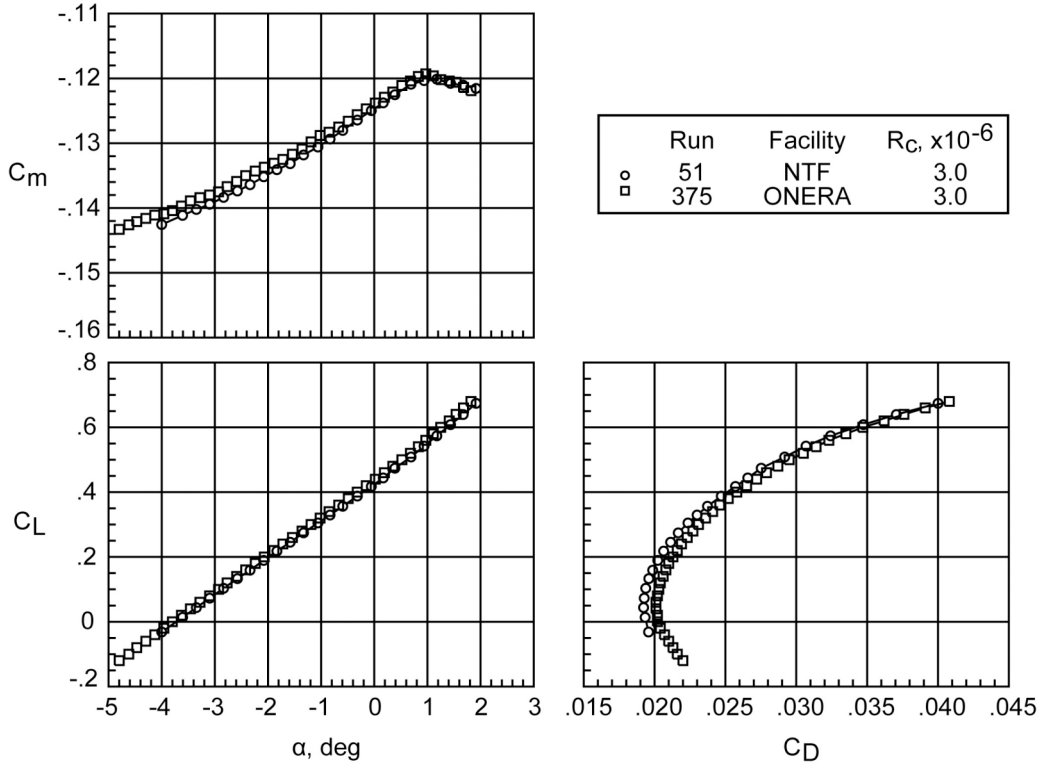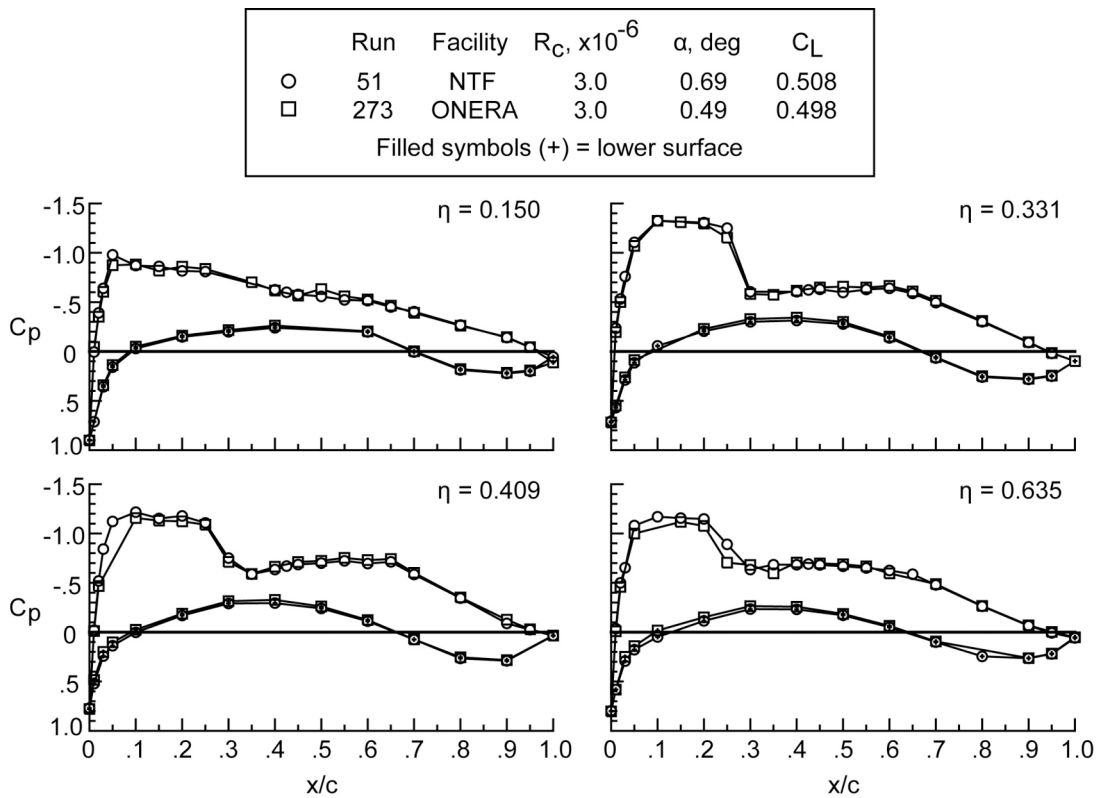**Figure 5. FX2B side-of-body fairing installed on the DLR-F6 model.**

Figure 6. DLR-F6 model components.

a) Longitudinal force and moment data.

	Run	Facility	R_C, x10^{-6}	α, deg	C_L
O	51	NTF	3.0	0.69	0.508
□	273	ONERA	3.0	0.49	0.498
	Filled symbols (+) = lower surface				

b) Wing surface pressure data.
Figure 7. Comparison of NTF and ONERA data for the Wing/Body configuration.

American Institute of Aeronautics and Astronautics
092407
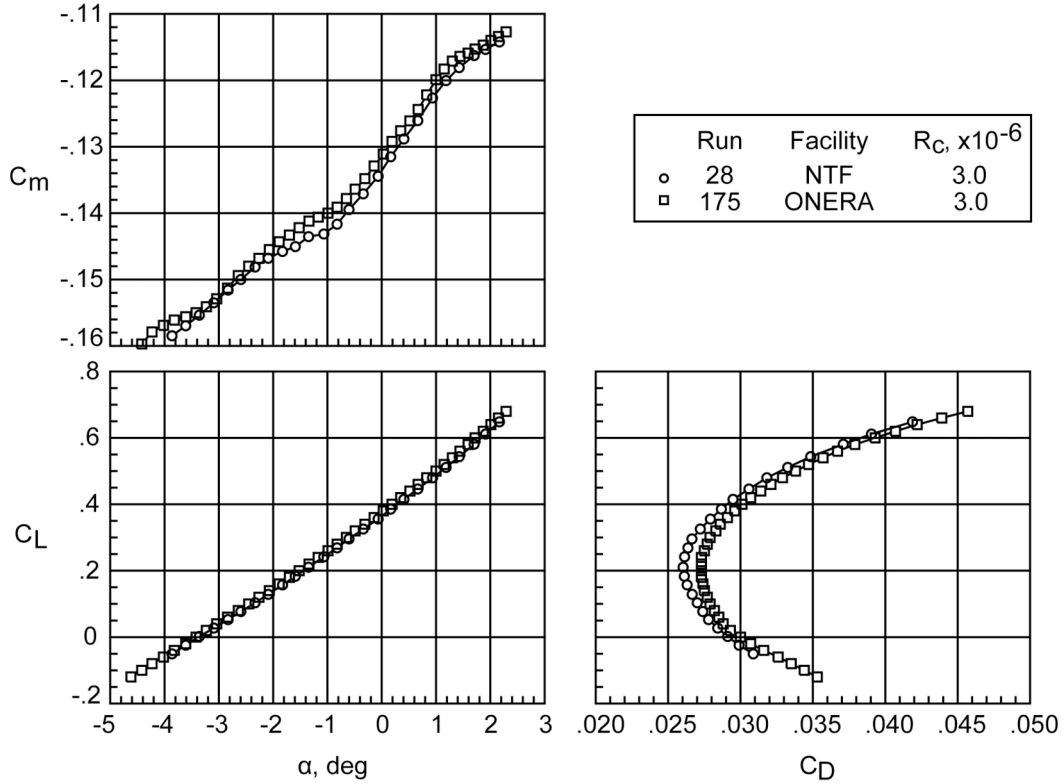
a) Longitudinal force and moment data.
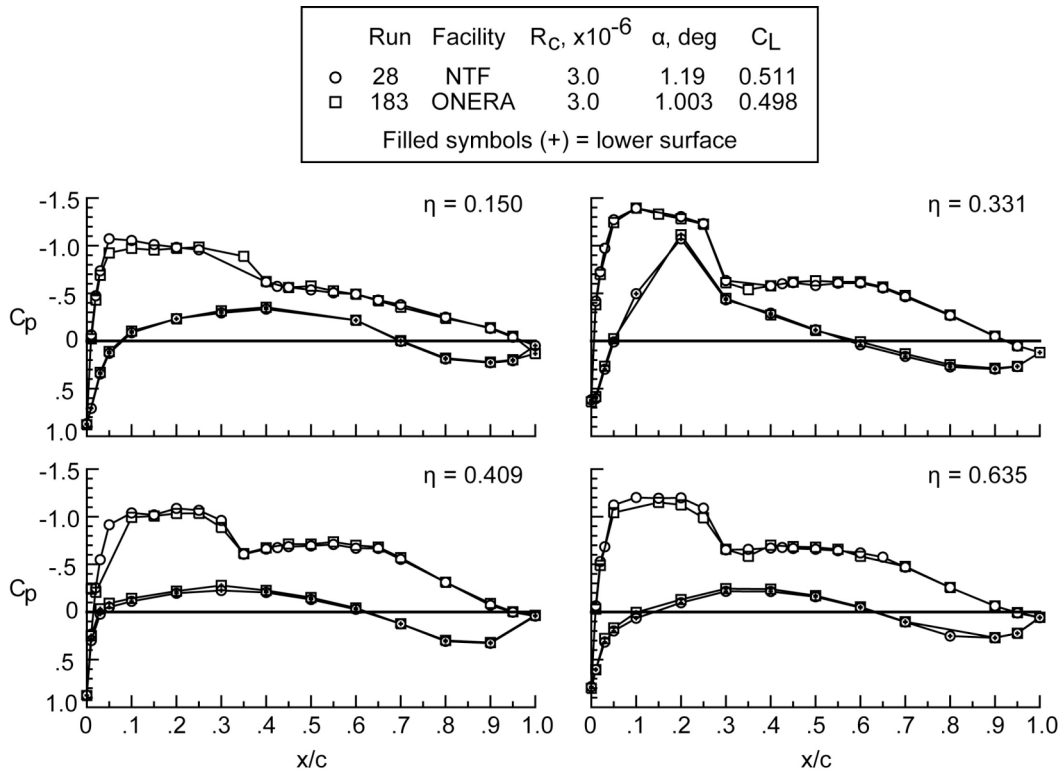
b) Wing surface pressure data.
Figure 8. Comparison of NTF and ONERA data for the Wing/Body/Nacelle/Pylon configuration.

American Institute of Aeronautics and Astronautics
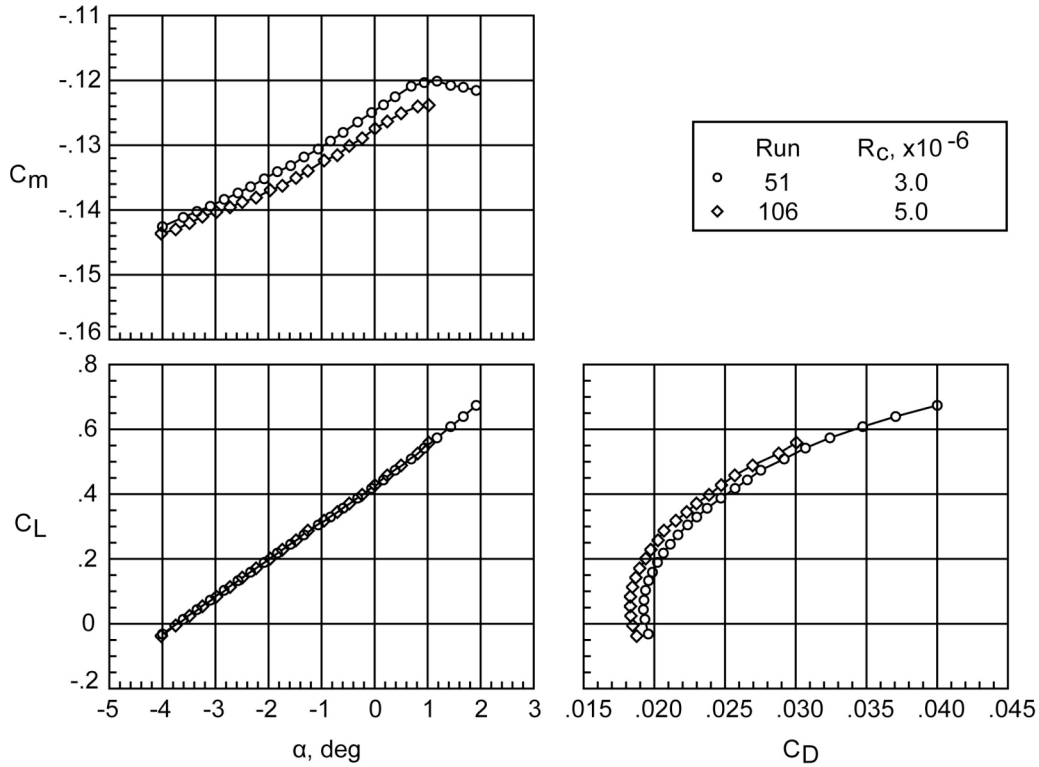
a) Longitudinal force and moment data.
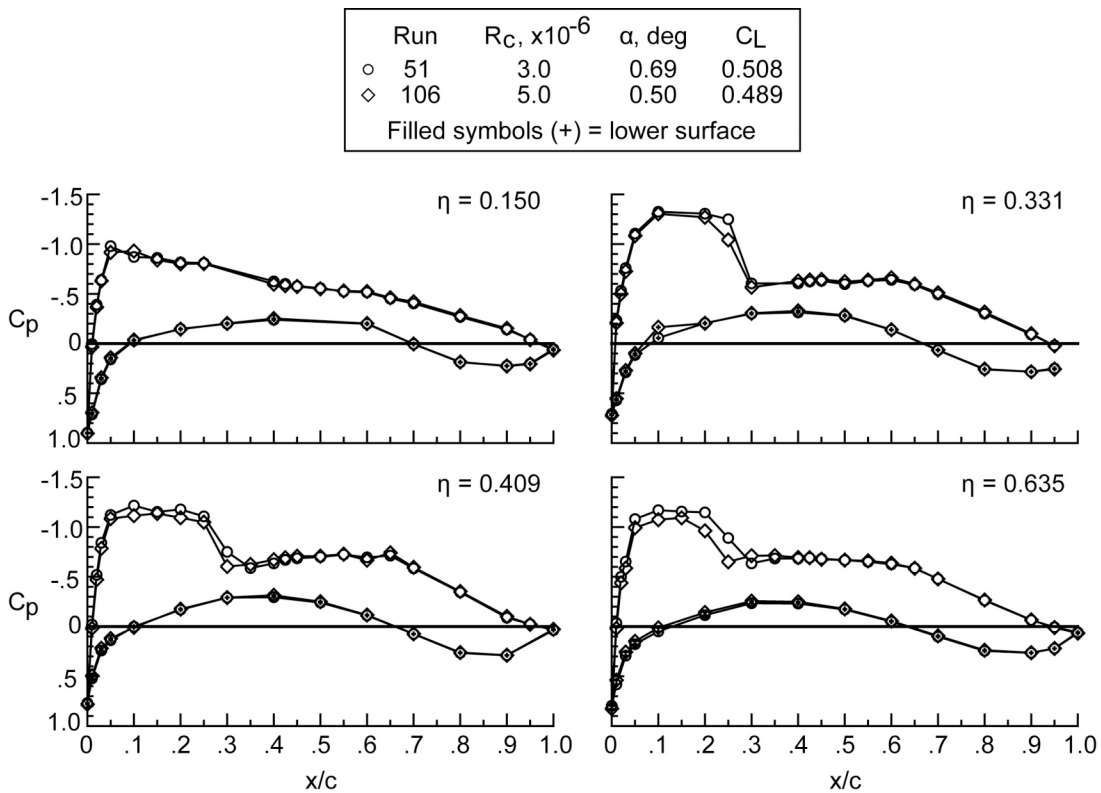
b) Wing surface pressure data.

Figure 9. Reynolds number effects for the Wing/Body configuration, NTF data only.

15
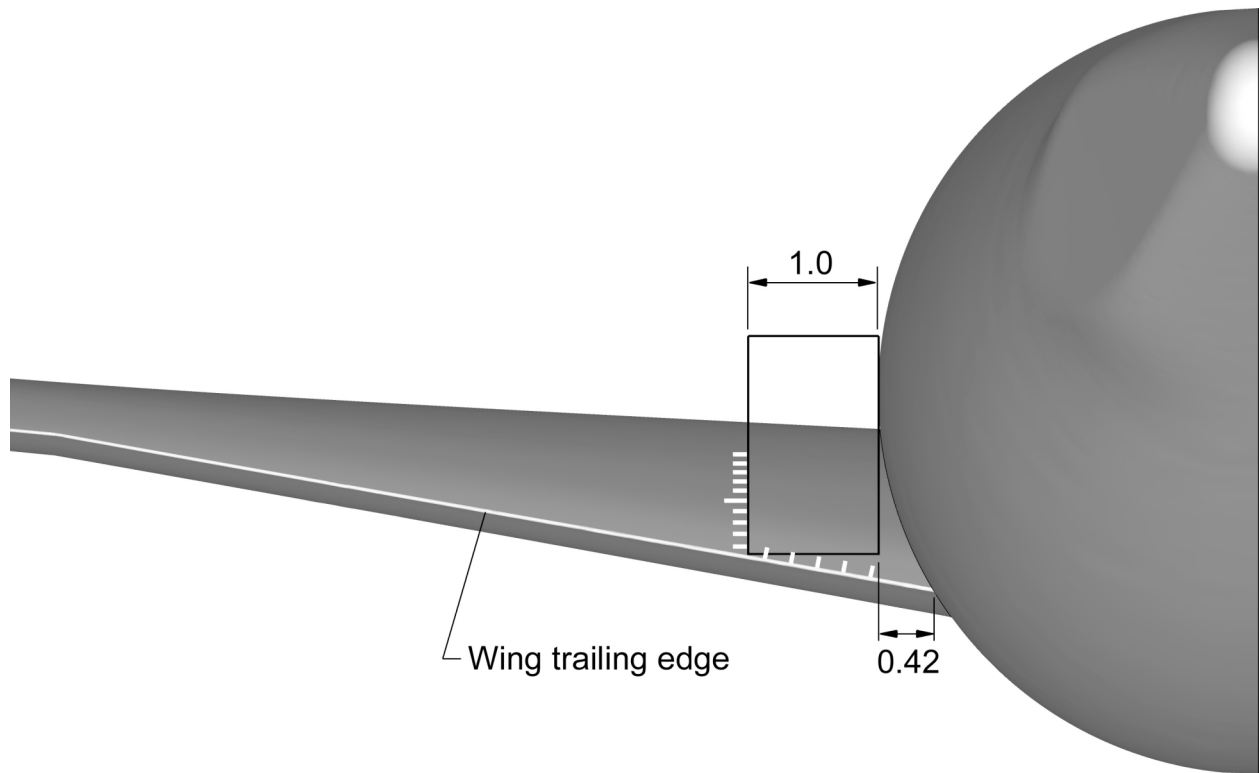
Figure 10. Details of tick mark layout for flow visualization. Dimensions are given in inches.
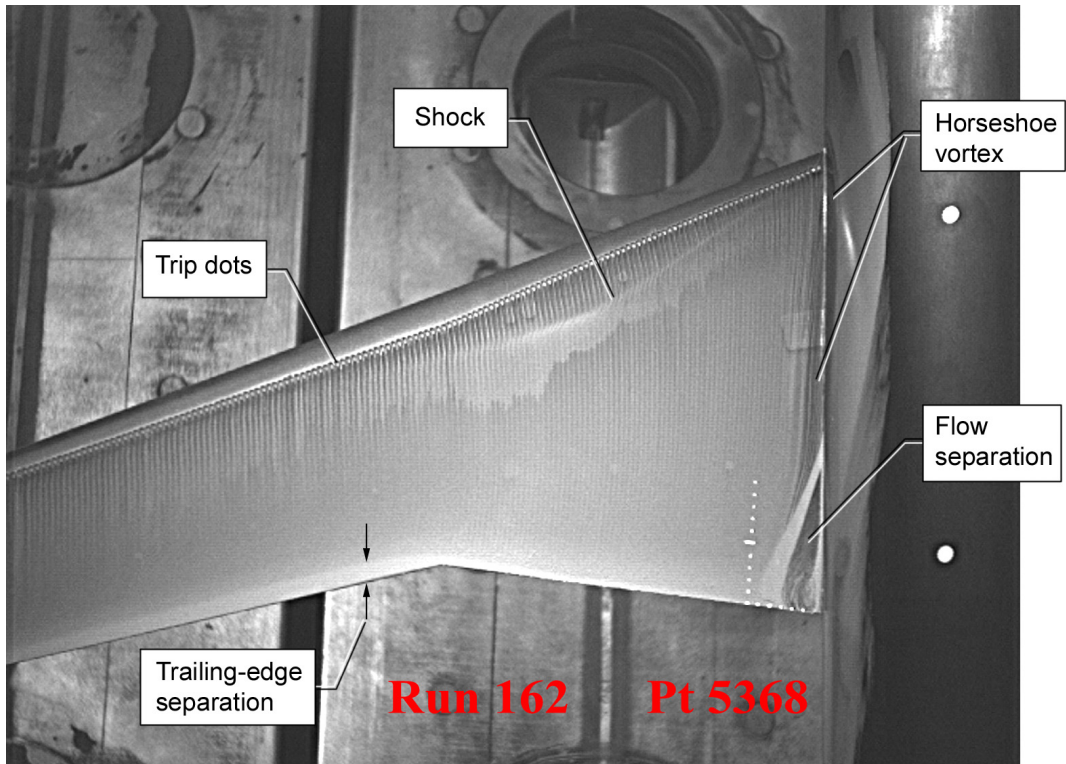
a) R_c = 3 million.
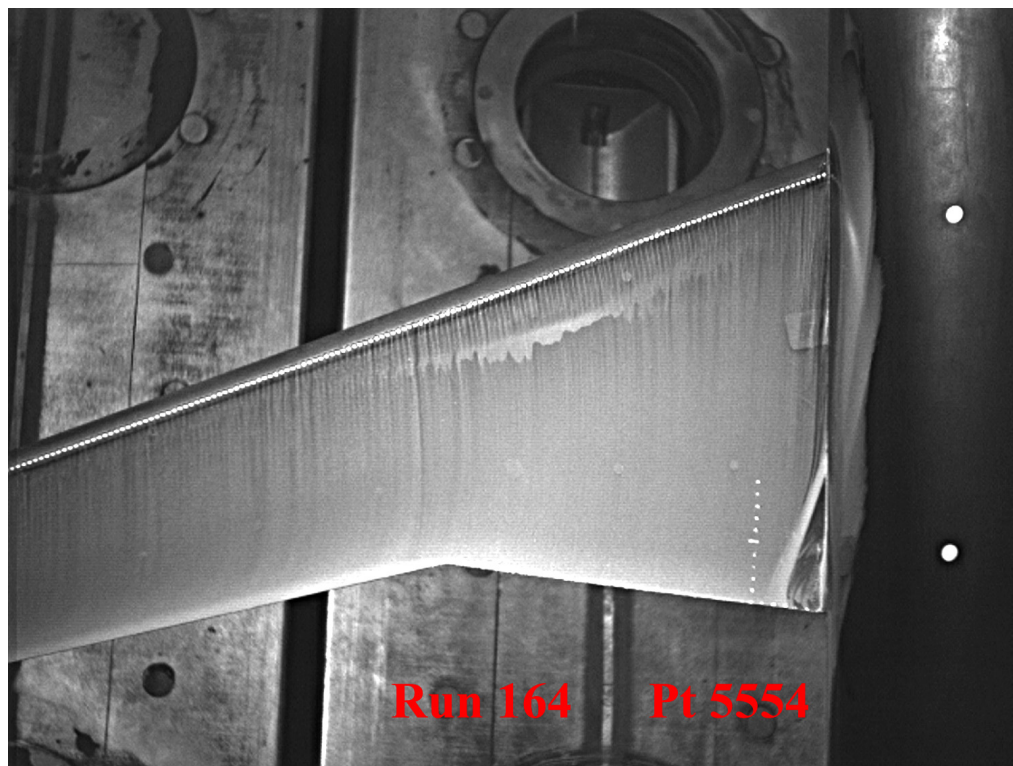
b) R_c = 5 million.

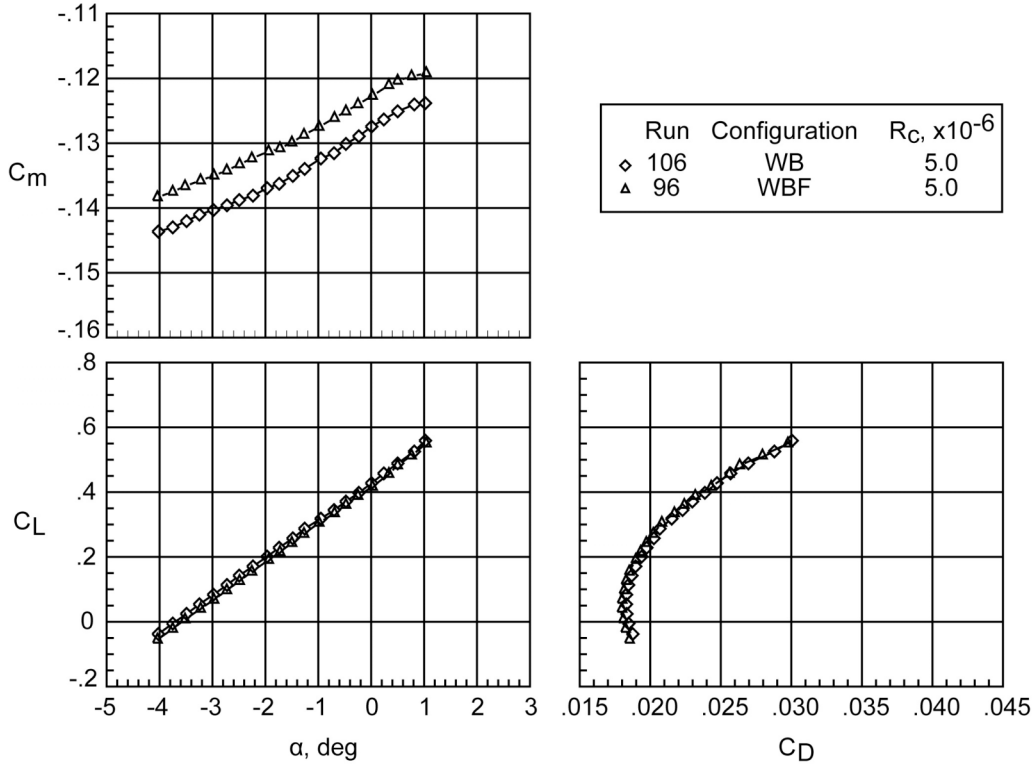**Figure 11. Surface oil flow visualization on the Wing/Body configuration, C_L = 0.5, top inboard view.**
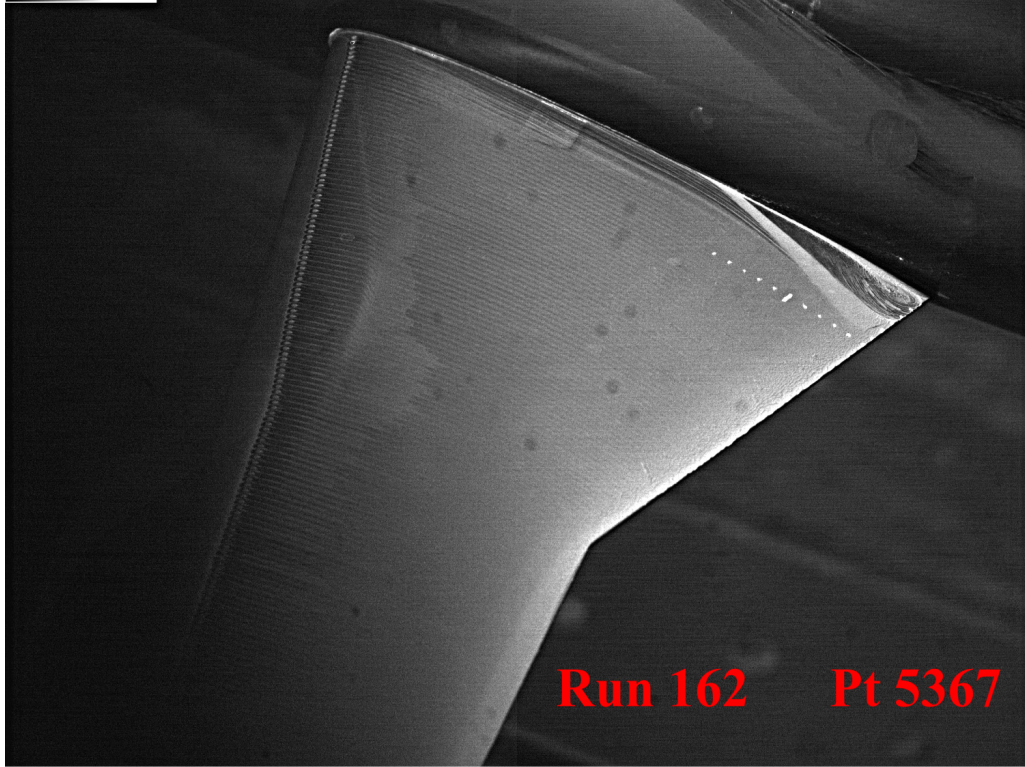
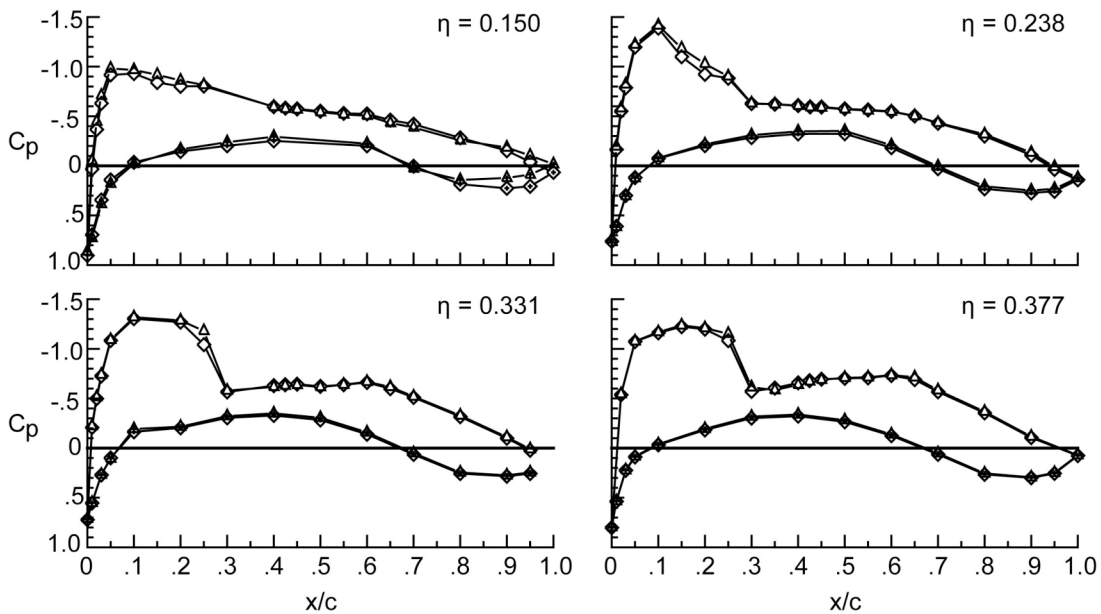a) R_c = 3 million.
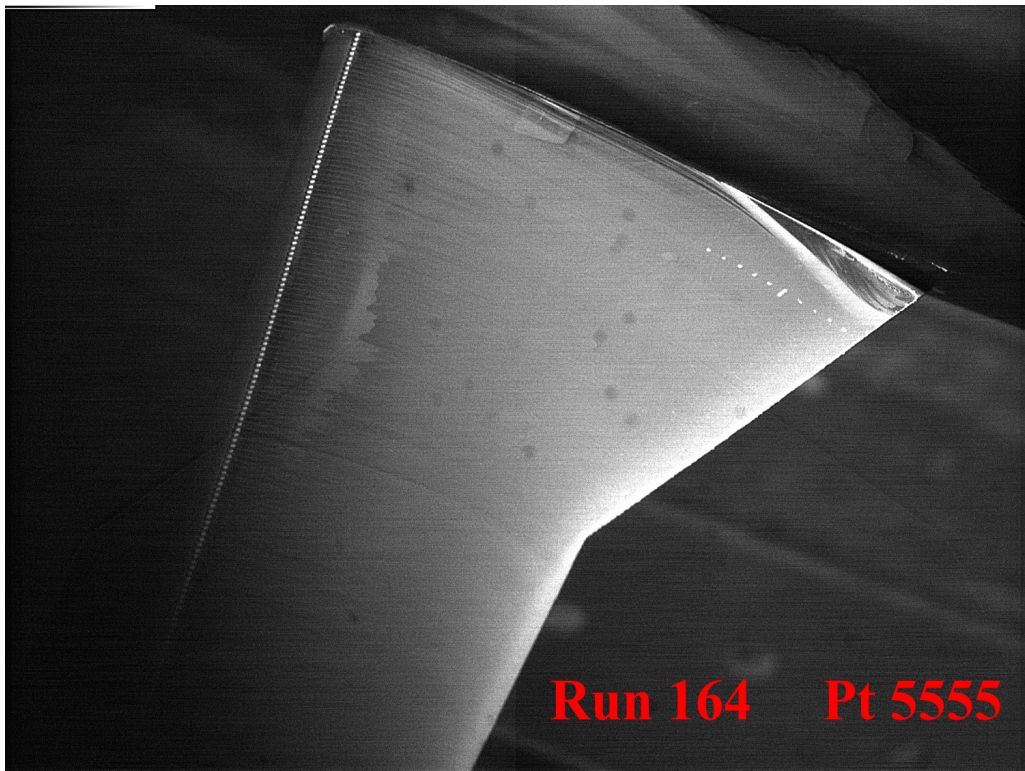
b) R_c = 5 million.
Figure 12. Surface oil flow visualization on the Wing/Body configuration, C_L = 0.5, rear ¾ view.

Figure legend (top plot):

	Run	Configuration	R_c, $x10^{-6}$
◇	106	WB	5.0
△	96	WBF	5.0

a) Longitudinal force and moment data.

Figure legend (bottom plots):

	Run	Configuration	R_c, $x10^{-6}$	α, deg	C_L
◇	106	WB	5.0	0.50	0.489
△	96	WBF	5.0	0.50	0.483

Filled symbols (+) = lower surface

b) Wing surface pressure data.
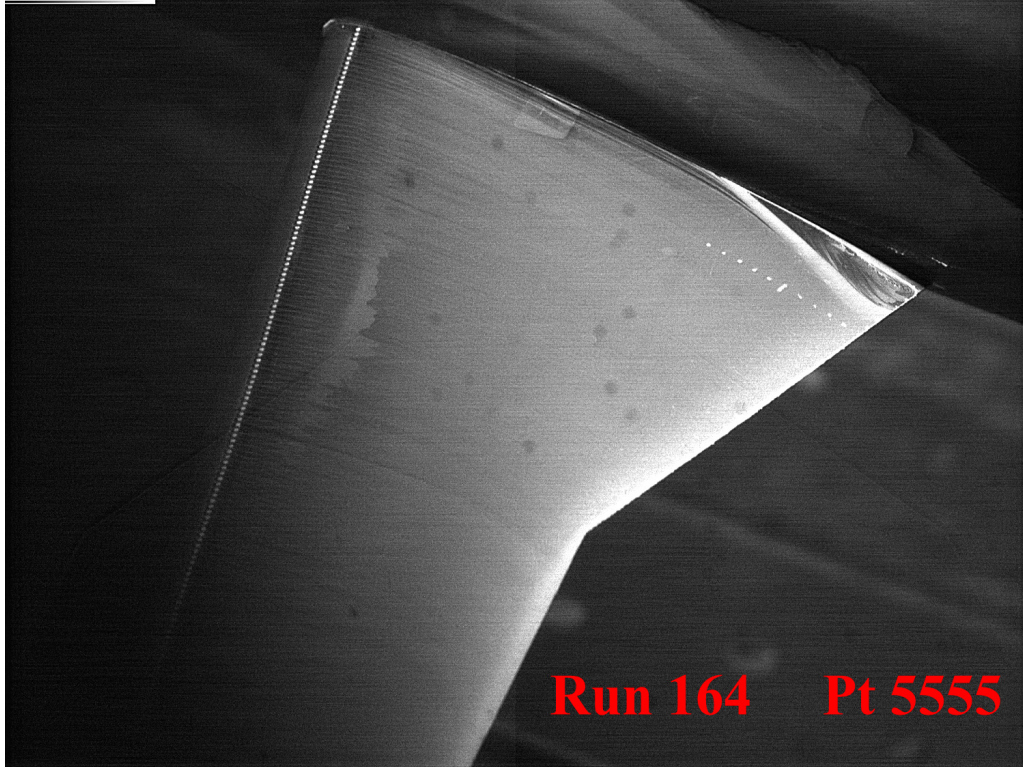Figure 13. Effects of adding the FX2B fairing, NTF data only.

American Institute of Aeronautics and Astronautics
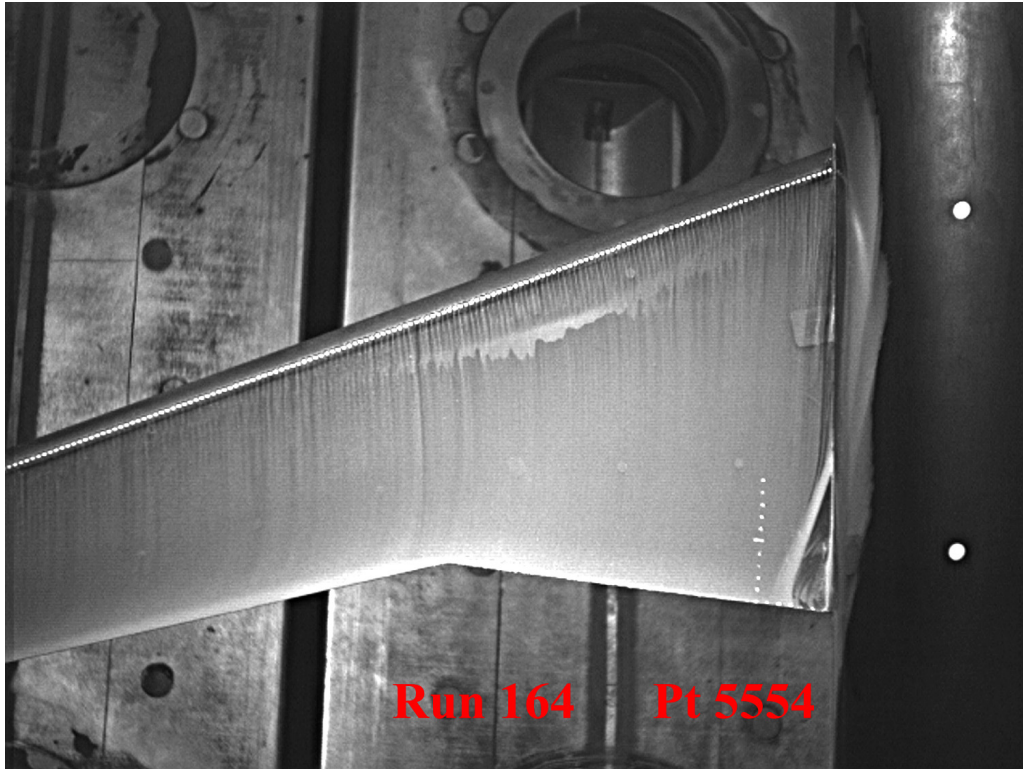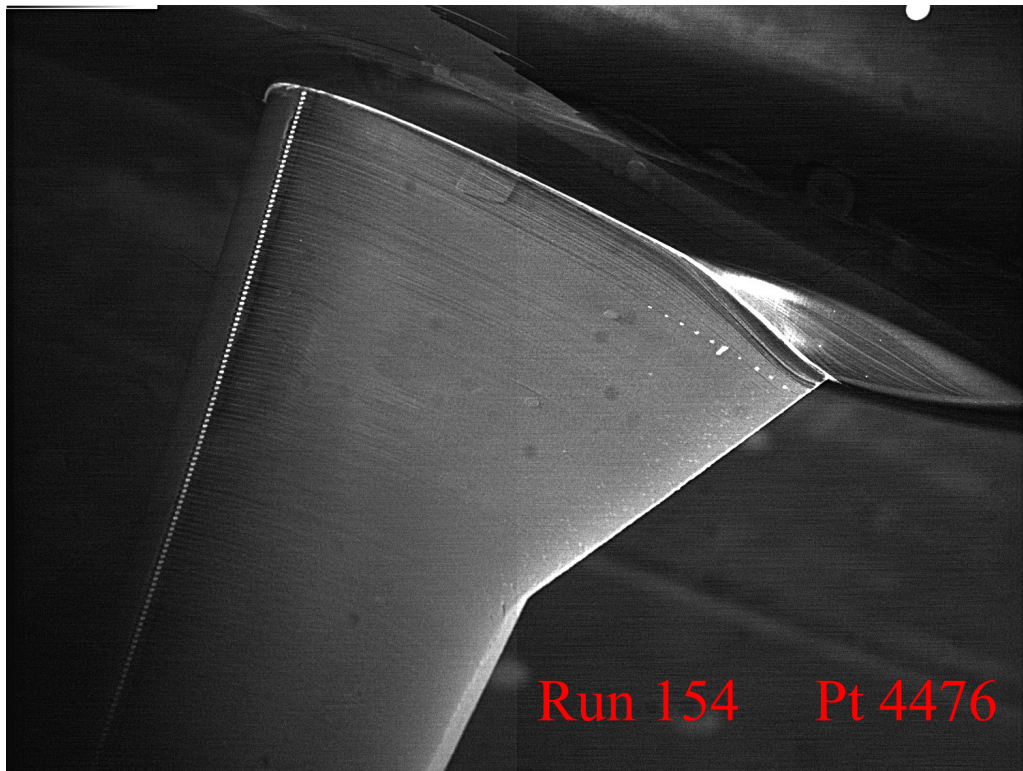
a) Wing/Body configuration.

b) Wing/Body/Fairing configuration.
Figure 14. Surface oil flow visualization showing the effects of the FX2B fairing, $C_L = 0.5$, top inboard view.

Run 164   Pt 5555

a) Wing/Body configuration.

Run 154   Pt 4476

b) Wing/Body/Fairing configuration.
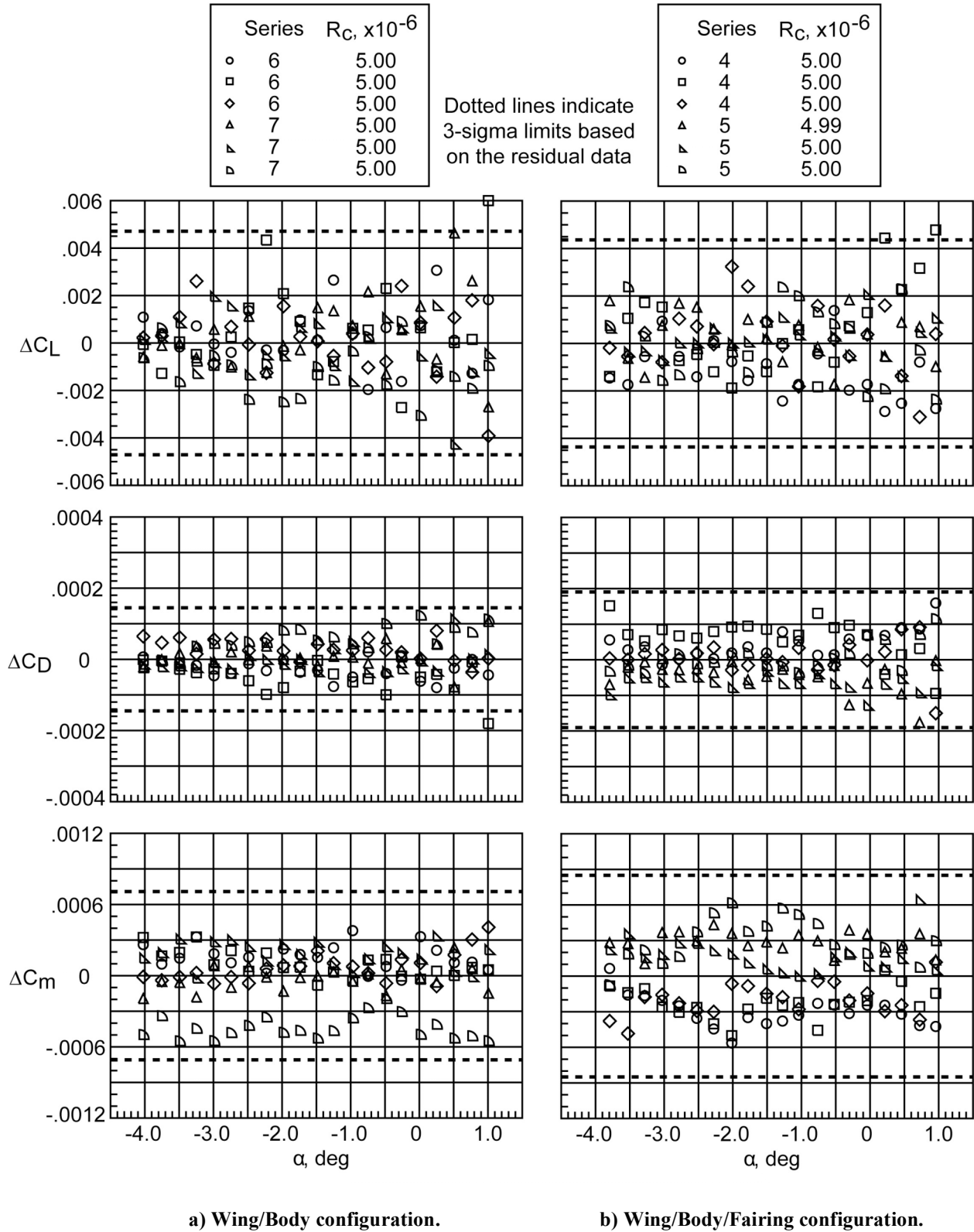**Figure 15. Surface oil flow visualization showing the effects of the FX2B fairing, C_L = 0.5, rear ¾ view.**

Figure 16. Data Repeatability.

a) Wing/Body configuration.   b) Wing/Body/Fairing configuration.

092407